Lidar and Pressure Measurements of Inner-Surfzone Waves and Setup

K. L. BRODIE

Coastal and Hydraulics Laboratory, U.S. Army Engineer Research and Development Center, Duck, North Carolina

B. RAUBENHEIMER AND STEVE ELGAR

Woods Hole Oceanographic Institution, Woods Hole, Massachusetts

R. K. SLOCUM AND J. E. MCNINCH

Coastal and Hydraulics Laboratory, U.S. Army Engineer Research and Development Center, Duck, North Carolina

(Manuscript received 9 December 2014, in final form 10 July 2015)

ABSTRACT

Observations of waves and setup on a steep, sandy beach are used to identify and assess potential applications of spatially dense lidar measurements for studying inner-surf and swash-zone hydrodynamics. There is good agreement between lidar- and pressure-based estimates of water levels ($r^2 = 0.98$, rmse = 0.05 m), setup ($r^2 = 0.92$, rmse = 0.03 m), infragravity wave heights ($r^2 = 0.91$, rmse = 0.03 m), swell–sea wave heights ($r^2 = 0.87$, rmse = 0.07 m), and energy density spectra. Lidar observations did not degrade with range (up to 65 m offshore of the lidar) when there was sufficient foam present on the water surface to generate returns, suggesting that for narrow-beam 1550-nm light, spatially varying spot size, grazing angle affects, and linear interpolation (to estimate the water surface over areas without returns) are not large sources of error. Consistent with prior studies, the lidar and pressure observations indicate that standing infragravity waves dominate inner-surf and swash energy at low frequencies and progressive swell–sea waves dominate at higher frequencies. The spatially dense lidar measurements enable estimates of reflection coefficients from pairs of locations at a range of spatial lags (thus spanning a wide range of frequencies or wavelengths). Reflection is high at low frequencies, increases with beach slope, and decreases with increasing offshore wave height, consistent with prior studies. Lidar data also indicate that wave asymmetry increases rapidly across the inner surf and swash. The comparisons with pressure measurements and with theory demonstrate that lidar measures inner-surf waves and setup accurately, and can be used for studies of inner-surf and swash-zone hydrodynamics.

1. Introduction

The maximum run-up elevation, defined as the highest location the ocean water reaches on the beach, affects storm impacts on coasts (Sallenger 2000; Stockdon et al. 2007; Masselink and van Heteren 2014). The maximum run-up level depends on (i) the increase in the mean sea level owing to breaking waves (known as wave setup) and (ii) the excursion of the wave-driven ocean–beach intersection (known as swash). These processes are affected by the transformation of infragravity and swell–sea waves across the surfzone and the bathymetry of the surfzone and foreshore. Wave setup can be significant, exceeding 1 m during storms, and alongshore gradients in wave setup, resulting from alongshore variations in wave forcing, can drive significant alongshore currents (Putrevu et al. 1995; Haller et al. 2002; Haas et al. 2003; Apotsos et al. 2008; Hansen et al. 2014). Infragravity waves may become trapped within the inner surfzone, inducing spatial variations in sediment transport direction associated with nodes and antinodes within the standing wave field (Beach and Sternberg 1988; Aagaard and Greenwood 1994). Bathymetric evolution of the inner surfzone can be rapid, varying in both space and time over the course of a storm, as cross-shore undertow, alongshore currents, and oscillatory incident- and infragravity-wave-driven flows interact

Corresponding author address: Katherine L. Brodie, Coastal and Hydraulics Laboratory, U.S. Army Engineer Research and Development Center, 1261 Duck Rd., Duck, NC 27949.
E-mail: katherine.l.brodie@usace.army.mil

with each other and with evolving morphology to change sediment transport magnitude and direction (Aagaard and Greenwood 1994; Houser et al. 2006; Houser and Greenwood 2007). Accurate measurements of these inner-surf and swash-zone hydrodynamic processes, as well as bathymetric change, are critical to improving models for nearshore hydrodynamics, the resulting sediment transport, and the erosion and recovery of coasts during and following storms (van Rooijen et al. 2012; Kobayashi and Jung 2012).

Setup and surfzone waves typically have been measured using nearbed pressure sensors (Guza and Thornton 1982; King et al. 1990; Lentz and Raubenheimer 1999; Raubenheimer et al. 2001; Apotsos et al. 2008), nearbed manometer tubes (Nielsen 1988; Jafari et al. 2012), or surface-piercing resistance wire gauges (Battjes and Stive 1985). Setup in the swash zone also has been measured using video-based tracking of the water–beach intersection (Holman and Sallenger 1985). More recently, processes in the swash zone have been observed with laser techniques (Blenkinsopp et al. 2010; Brodie et al. 2012; Almeida et al. 2013; Vousdoukas et al. 2014).

A lidar scanner can be mounted above the water on the beach or dune, enabling remote measurements of the water surface and the uncovered beach between swashes. Thus, lidar can be set up rapidly before a storm, or in locations with large plunging waves, for which deployment of in situ sensors is difficult. The water surface elevation is measured directly, and thus attenuation through the water column need not be considered (as it is for nearbed sensors), and sand-level changes can be measured when the beach is uncovered by swashes. Laser scanners accurately measure the subaerial beach topography in and shoreward of the swash zone in large-scale laboratory (Almeida et al. 2013; Vousdoukas et al. 2014) and field (Brodie et al. 2012) studies. Lidar estimates of swash heights and excursions agree well with pressure and video estimates (Blenkinsopp et al. 2010; Almeida et al. 2013; Vousdoukas et al. 2014). Instantaneous swash profiles measured with a lidar were correlated with those from an array of ultrasonic sensors (Puleo et al. 2014). Inner-surf wave heights estimated with lidar in large-scale laboratory studies are within about 10% of in situ measurements (Blenkinsopp et al. 2012; Vousdoukas et al. 2014). However, there have been few field evaluations of lidar measurements of waves and water levels offshore of the swash zone. Here, low-grazing angle lidar is used in the field to measure the water surface from the swash across the inner surf-zone. Lidar- and pressure-sensor-based observational estimates of wave statistics, spectra, and setup are
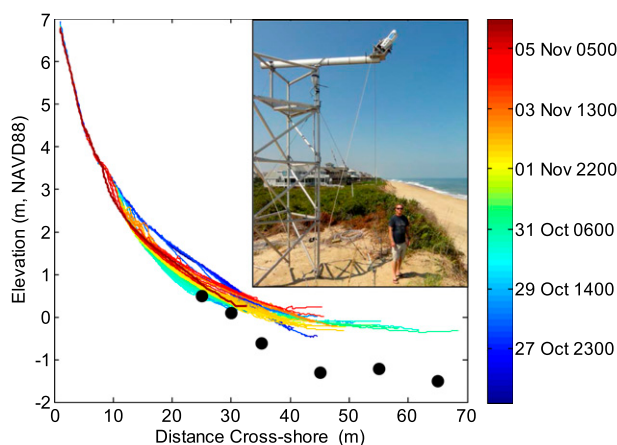

FIG. 1. Elevation of the sand surface [curves, colors (scale on the right) indicate time with blue representing the start of the experiment and red the end] vs cross-shore distance. Filled black circles are locations of the buried pressure gauges. The lidar was at distance = 0 m. The inset shows a photograph of the lidar setup.

compared with each other. Potential applications of the spatially dense lidar observations for investigating inner surf-zone hydrodynamics also are explored.

2. Field site and instrumentation

Observations of waves in the inner surf and swash, mean water levels, and swash-zone sand levels were acquired from 26 October to 7 November 2011 on a sandy Atlantic Ocean beach near Duck, North Carolina, using a combination of in situ pressure gauges and a lidar mounted on a tower on the dune (Fig. 1). Sand levels, instrument locations, and the tops of mounting pipes were measured at all in situ sensors (referred to by cross-shore distance from the lidar, so gauge g25 is 25 m seaward of the lidar) immediately after deployment using a postprocessed GPS system (accuracy of 0.02 m). Sand levels at instruments shoreward of about the midswash also were measured by hand relative to the tops of the mounting pipes during daytime low tides (not shown), and swash-zone sand levels were estimated from the lidar data during every run (Fig. 1; see below for details). This methodology provided frequent sand-level estimates at the shallowest gauges, but few measurements at the deepest gauges (g55 and g65), which nearly always were covered by water (except at the lowest spring tides during periods of small waves). Errors in the estimated sand levels could contribute to errors in the wave heights estimated from the pressure gauges (see section 4). Sand levels above g25 and g30 were roughly constant from 26 October until 0800 eastern daylight time (EDT) 28 October (dark blue curves in Fig. 1), decreased from 28 October to a minimum at 1400 EDT 30 October
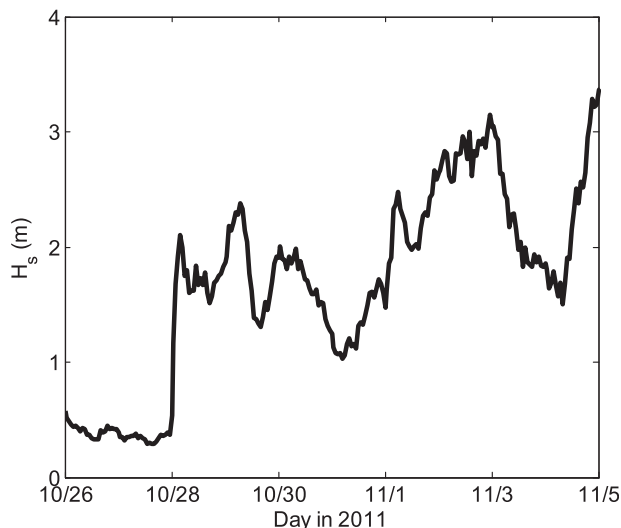
FIG. 2. Significant wave heights in 5-m water depth vs time.

(blue through green curves), and then increased until 0700 EDT 3 November (green through orange-red curves), before decreasing at the end of the experiment (5 November, dark red curve). Sand levels above the offshore gauges (g35–g65) were measured more intermittently by the lidar, but they typically increased from the start of the experiment until 1400 EDT 29 October (blue through cyan curves), and then decreased until 0100 EDT 2 November (green through yellow curves), before increasing through the end of the experiment (5 November, orange through red curves). Beach slope, defined as the best-fit linear trend within the swash zone, ranged between 0.02 and 0.17 during the experiment. Rapid bed elevation changes of up to 0.25 m over 20 min near 0800 EDT 28 October were associated with high tide and increasing offshore wave energy (Fig. 2). The lidar observations are qualitatively consistent with the hand-measured sand levels (not shown).

The tidal range was about 1 m. Offshore (5-m water depth) significant wave heights (4 times the standard deviation of sea surface elevation fluctuations), wave directions, and centroidal frequencies in the swell–sea frequency (f) band ($0.05 < f < 0.25$ Hz) ranged from 0.5 to 3.0 m (Fig. 2), 20° to 90° true north (shore normal is 72° true north), and 0.07 to 0.25 Hz, respectively. Large amounts of seaweed toward the end of the experiment occasionally interfered with lidar observations of the swash, and those observations were removed from the analysis.

Setup (setdown) is defined here as the increase (decrease) of the mean water level relative to that observed (with the same type of instrument, pressure,

or lidar) water level at the location of the most offshore sensor, g65. Maximum setup in the swash was about 0.6 m.

a. Lidar system

A Riegl terrestrial lidar scanner (LMS-z390i, 1550-nm laser with a 0.3-mrad beamwidth) was used to measure water and sand levels at 4 Hz with a 0.02° angular resolution for 20 min starting at the top of each hour. The lidar, which was mounted on a 4-m scaffolding tower on the crest of the dune (Fig. 1, inset), calculates distances from the time for a pulsed laser beam to travel to a target and back. To conduct a ''line scan'' along a narrow vertical profile, the laser beam is deflected vertically by a spinning prism of mirrors that continuously rotates. The lidar was mounted at a 30° downward angle relative to the horizontal to ensure the dune toe was in the ±40° field of view (Fig. 1, inset). The mounting geometry resulted in a low angle of incidence to the flat water surface, and therefore returns are recorded only when the laser beam diffusely reflects off breaking waves, relict foam on flat water surfaces, or when the steep faces of incoming waves allow for direct specular reflection of the laser beam back toward the scanner. Wet surfaces absorb much of the laser energy at the near-infrared wavelengths, and thus returns from the water surface have significantly lower amplitudes than returns from dry land. The maximum range of the measurements depends on environmental conditions (wave breaking, foam, rain, fog, spray) and on the return detection thresholds set by the manufacturer, and rarely exceeded 150 m for this experiment. For the setup used here, the 0.3-mrad beam illuminates a 0.004-m-diameter (0.237) spot on a horizontal plane at an elevation of 0-m North American Vertical Datum of 1988 (NAVD88) that is 5 (100) m from the lidar. Spot size is considerably smaller if the beam intersects a perpendicular surface, ranging from 0.001 to 0.031 m between 5 and 100 m from the lidar. These spot sizes are typically smaller than the wave height and wavelength, and thus errors related to spot size are expected to be small.

Drawbacks to the lidar include attenuation in heavy rain or fog, particularly for single-return scanners, such as the LMS-z390i, and shadowing of the backside of incoming waves owing to the low grazing angle (interpolation may be required to estimate the full free-surface profile). In addition, returns can be sparse on the foreshore immediately following rundown when a thin film of water is left on the beach surface, causing specular reflection of the laser beam away from the lidar. Small tilts (e.g., 0.01°) or movement in the lidar mounting platform can lead to errors in elevation and

position of the water and sand surfaces, especially at long ranges. Techniques to measure and correct for these small-scale changes in orientation of the scanner using coregistration algorithms will be discussed in future work, and were not applied in this study. Here, field precision was roughly ±0.015 m, about twice the manufacturer specifications, and was determined by analyzing time series of lidar returns from the stationary dry beach.

To estimate foreshore slopes, run-up, and wave statistics, data were transformed from the scanner coordinate system (angle and range) to rectified Cartesian coordinates (local coordinates for the horizontal and NAVD88 coordinates for the vertical) using a transformation matrix determined from scans of GPS-surveyed reflectors. Time differences between the first and last data point within a single line scan are small (0.12 s), and therefore all points within that scan were assigned the same time. Each line scan was then interpolated to 0.10-m resolution in the cross-shore. To separate foreshore points from water surface points, the line-scan elevation data were analyzed similarly to an Argus wave run-up time stack (Holman et al. 1993), but instead of identifying a color threshold, an elevation threshold was used. Sand-level changes on the lower foreshore occur on the time scale of infragravity and swell–sea waves (Howd and Holman 1987), and thus running minimum filters with time windows ranging from 1.2 to 30.0 s were used to generate multiple temporally varying minimum surfaces. Each minimum surface was subtracted from the original line-scan elevation data, and the resulting difference maps for all minimum surfaces were averaged. For each line scan, the most shoreward location with an elevation > 0.015 m above the average minimum surface was identified as the run-up–beach intersection (the maximum run-up location), with seaward points classified as water and landward points identified as the foreshore. The run-up extraction algorithm correctly separated water and land points only 85% of the time, because relict foam or seaweed often interfered with the digitizing, and therefore each collection was checked by hand to ensure proper separation of water and land points. A ''mean foreshore profile'' for each 20-min collection was calculated by averaging the instantaneous foreshore elevations (land points) at each cross-shore location over the 20-min collection and was used to update pressure sensor burial measurements when applicable (see below).

For spectral and time series analysis, each 20-min lidar collection was divided and segmented into two 512-s (8.5 min) sections. Mean water level is defined as the time-averaged water level for each section of data.

Significant wave heights in the total ($0.004 < f < 0.250$ Hz), infragravity ($0.004 < f < 0.050$ Hz), and swell–sea ($0.050 < f < 0.250$ Hz) bands were estimated from the area under the frequency spectrum.

b. In situ pressure gauges

The pressure sensors were buried (initially about 0.50–0.75 m) to avoid flow-induced deviations from hydrostatic pressure (Raubenheimer et al. 2001). Pressure measurements were collected at 2 Hz for 51.2 min, starting at the top of each hour. Mean water levels were calculated from the surveyed sensor location and the time-averaged 512-s pressure measurements assuming hydrostatic pressure and a water density of 1020 kg m^{-3}. Results were not sensitive to the chosen density value in these shallow-water depths. Effects of temperature changes on the pressure measurements were compensated with internal temperature sensors. Pressure gauge g35 did not start operating until 1 November.

The GPS-measured vertical locations of g35, g45, and g55 were adjusted (by less than 0.05 m) to ensure that the mean sea level was ''flat'' with respect to g65 over the 512-s runs starting 1934 EDT 26 October, 0800 EDT 27 October, and 2025 EDT 27 October, when tide levels were high and offshore wave heights (in 5-m water depth) were less than 0.35 m. Comparisons of hand-measured sand level above the buried pressure gauges with ''sand level'' estimated from the observations between swashes assuming hydrostatic pressure and saturated sand agreed within the measurement error of ~0.02 m for these techniques (Raubenheimer et al. 2001).

Sea surface fluctuations were estimated from the pressure measurements using linear wave and poroelastic theories to account for the attenuation of pressure fluctuations through the water and the saturated sand above the buried sensors, respectively [Raubenheimer et al. 1998, Eq. (5)]. Similar to the lidar observations, significant wave heights in the total, infragravity, and swell–sea bands were estimated from the frequency spectrum. Water and burial depths were estimated from the sand levels determined by the lidar and by hand measurements at in situ gauges in the swash at low tide.

3. Lidar–pressure comparisons

For comparison with the in situ measurements, the lidar time series were decimated to 2 Hz prior to frequency-domain filtering and prior to estimating water levels or wave heights. Only the two 512-s sections of in situ data that were collected at the top of each hour are included in the comparisons. If the beach is not saturated, then a pressure gauge will measure the

TABLE 1. Squared correlation (r^2), rmse, bias, and the best-fit linear slope between lidar and pressure measurements of mean water level, setup, and significant wave height (H_s). Statistics for significant wave height in the swell-sea band are provided for individual locations to illustrate gauge-dependent trends. All p values were less than 0.001.

	r^2	Rmse (m)	Bias (m)	Slope
Mean water level	0.98	0.05	−0.07	1.1
Setup	0.92	0.03	−0.01	1.1
H_s (total)	0.85	0.09	0.12	0.9
H_s (infragravity)	0.91	0.03	0.03	1.0
H_s (swell-sea)	0.87	0.07	0.08	0.9
H_s (swell-sea) g25	0.77	0.06	0.10	0.9
H_s (swell-sea) g30	0.84	0.06	0.04	1.0
H_s (swell-sea) g35	0.88	0.05	0.09	1.1
H_s (swell-sea) g45	0.96	0.04	0.03	1.3
H_s (swell-sea) g55	0.97	0.04	−0.04	1.1
H_s (swell-sea) g65	0.93	0.05	−0.06	1.1

groundwater pressure head, rather than the height of the swash or wave above the beach. Therefore, comparisons were conducted only for locations offshore of the mean swash (see section 4). For comparing water levels, setup, and wave heights, the lidar and the pressure-gauge data were time synced using cross correlation to correct for clock drift, and squared correlation (r^2), root-mean-square error (rmse), mean bias, and best-fit linear slope statistics were calculated on overlapping portions of the time series (Table 1).

Mean water levels (relative to NAVD88) measured with the lidar and with the pressure gauge (Fig. 3a) are well correlated ($r^2 = 0.98$; Table 1). The mean water level estimated with the lidar is slightly lower (bias of −0.07 m; Table 1) than that estimated with the pressure gauges, especially for the most offshore locations and lowest water levels, possibly owing to a small tilt in the lidar tower over the course of the experiment that was not accounted for in the processing. Alternatively, the pressure measurements may be over-estimating the mean water level owing to slight errors in the measured vertical location of the instruments or the process for adjusting those locations to provide a flat sea surface (see section 2b). Although laboratory comparisons of lidar with in situ sensors have suggested that lidar may underestimate slightly the mean water level (Vousdoukas et al. 2014), especially when looking toward the oncoming waves (Blenkinsopp et al. 2012), the cause of the (small) water-level differences shown here is unclear (see section 4).

The lidar and pressure-estimated setup (Fig. 3b) are well correlated ($r^2 = 0.92$; Table 1). The low bias in the setup measurements suggests the cause of the bias in mean water level (Fig. 3a; Table 1) is specific to the instrument type (e.g., either a consistent error in processing

methods for all pressure gauges, or a consistent error in all the lidar measurements). However, the percent differences in the setup estimates can be significant, particularly for g25, which was often in the swash zone. For example, for a pressure-estimated setup of about 0.2 m (which is large offshore of the swash zone; Raubenheimer et al. 2001), the corresponding lidar estimate can range from 0.1 to 0.3 m (Fig. 3b). In addition, the setup estimated by the lidar typically is a few centimeters lower (higher) than that estimated with the pressure gauges at g45 (g30 and g35), possibly owing to errors in the vertical locations of the pressure gauges (and thus to the pressure-estimated setup), or to differences in lidar reflectivity or shadowing by waves between the inner surf and swash.

Significant wave heights (Fig. 4a) estimated with the pressure gauges and lidar agree well ($r^2 = 0.85$; Table 1). Relative to the pressure gauge, the lidar-based wave height estimates are slightly low at g65 and g55 and high at g25–g45. The higher lidar estimates of wave height at the shallower gauges may be owing to the presence of an aerated wave roller, which would increase the elevation of the water surface measured by the lidar, while not affecting the pressure measured by the gauge significantly. The lidar- and pressure-based infragravity wave heights (Fig. 4b) are somewhat more correlated ($r^2 = 0.91$; Table 1) than the total significant wave heights ($r^2 = 0.85$; Table 1). However, the lidar estimates are biased high relative to the pressure estimates at g25 (Fig. 4b, blue symbols; mean difference of 0.08). In the swell–sea band (Fig. 4c), lidar- and pressure-based estimates of wave height are well correlated ($r^2 = 0.87$; Table 1). However, the agreement is gauge dependent (Table 1). For example, differences increase with increasing wave height at g35, g45, g55, and g65 (best-fit linear slopes > 1.0; Table 1). Lidar and pressure estimates are somewhat less correlated at g25 ($r^2 = 0.77$; Table 1), and lidar estimates are biased high at the shallow gauges g25, g30, and g35 (offsets of 0.10, 0.04, and 0.09 respectively; Table 1) and low at the offshore gauges g55 and g65 (offsets of −0.04 and −0.06 respectively; Table 1). The low estimates by the lidar at the most offshore gauges may be owing to shadowing and drop outs in the far range of the lidar, whereas lower correlations at g25 may be related to water table effects within the swash zone (see section 4). Swell–sea wave height at a fixed location increases with increasing water depth, and thus the differences between the lidar- and pressure-based swell–sea wave heights also fluctuate with tidal level (not shown). The causes of these fluctuations are not clear, but they could include tidal changes in grazing angle, wave steepness, breaking wave type or shape, foaminess, and reflectivity that may affect
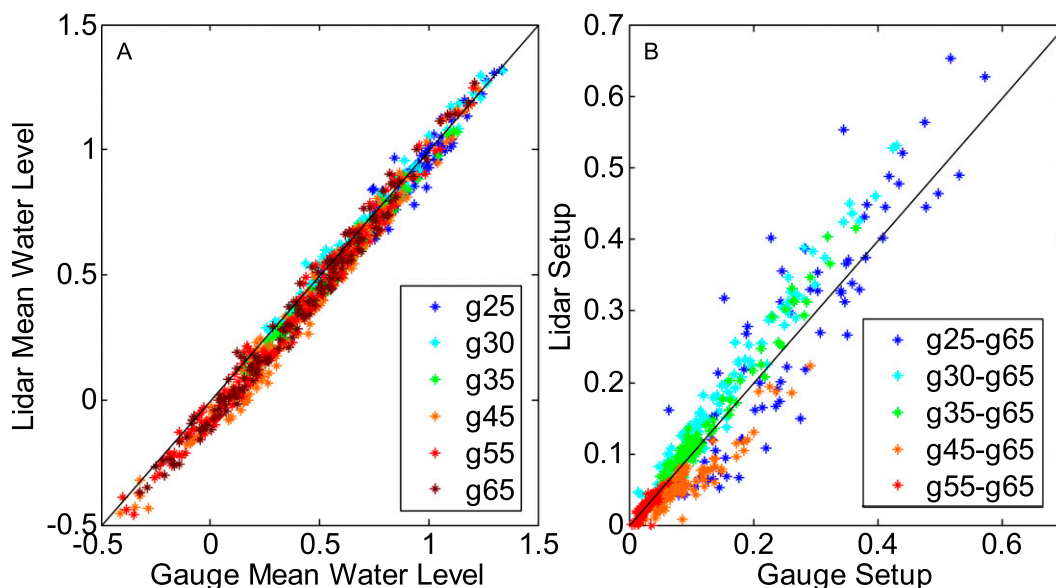
FIG. 3. Lidar vs pressure measurements of (a) the mean water level and (b) the wave setup at g25 (blue), g30 (cyan), g35 (green), g45 (orange), g55 (red), and g65 (purple).

the lidar measurements, or to tidal changes in vertical velocities (nonhydrostatic pressure) that may affect the pressure measurements. The sign of the difference is not consistent with tidal errors in the depth correction applied to the pressure measurements.

The shapes (e.g., locations of peaks and troughs) of the lidar energy density spectra are similar to the shapes of pressure-based spectra (Fig. 5). The wave energy levels estimated for $f \gtrsim 0.1\,\mathrm{Hz}$ at all locations except g30 are higher for the lidar measurements than for the pressure data (Fig. 5). In some cases, energy density differences are roughly constant with frequency, whereas in other cases differences are frequency dependent. Increasing errors with increasing frequency could indicate inaccurate bed-level estimates, and thus errors in transforming the buried pressure measurements to sea surface fluctuations (Raubenheimer et al. 1998; see section 4). Differences between energy densities estimated with the two sensing methods are roughly independent of frequency at g55 and g65 (Figs. 5e,f), consistent with the relatively good agreement of both infragravity (Fig. 4b) and swell–sea (Fig. 4c) wave heights at these locations.

The lidar- and pressure-based estimates of the wave phases relative to the shallowest sensor location are similar (Fig. 6) and show that the sea surface fluctuations are in phase or are 180° out of phase at low frequencies, as expected for standing waves (Guza and Thornton 1985). At higher frequencies ($\gtrsim 0.1\,\mathrm{Hz}$), the phases increase linearly with increasing frequency, as expected for progressive waves approaching the shore

(Raubenheimer et al. 1995). The ''cutoff'' frequencies below which standing waves dominate and above which progressive waves dominate depend on cross-shore location (and wave conditions). Close to the run-up limit (e.g., Figs. 6a,b; g30 and g35 for this high tide run) the waves are primarily standing. Farther from the shoreline (e.g., Fig. 6d,e; g55 and g65 for this run), the phases indicate the presence of progressive waves for frequencies greater than about 0.06 Hz.

4. Discussion

a. Sources of error

Potential sources of errors in the lidar measurements are related either to inaccuracies in the surface elevation measurements or to missing returns. Errors affecting the surface elevation measurements may result from the spatially variable lidar footprint (which changes with grazing angle and range), multiple reflections, or unknown movement of the scanner. For example, planar surfaces can appear convex owing to a combination of the spatially variable grazing angle, penetration into the water column, and the beam spread (Streicher et al. 2013). However, the longer wavelength light (1550 vs 905 nm) used here is absorbed strongly by water, reducing reflections from within the water column (Morel 1974). In addition, the relatively small lidar beam footprint used here (0.3 mrad) results in less spatial averaging than when using an 11.9-mrad footprint (Streicher et al. 2013). The lidar measurements also may have
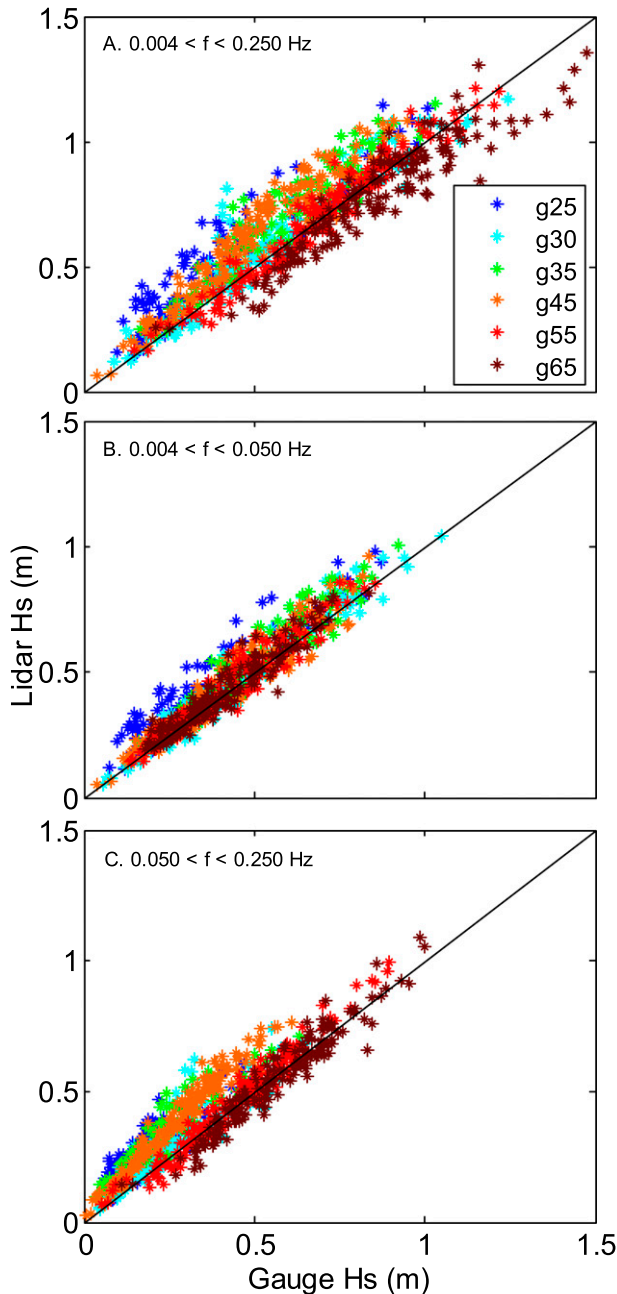
FIG. 4. Lidar vs pressure-estimated (a) total ($0.004 < f < 0.250$ Hz), (b) infragravity ($0.004 < f < 0.050$ Hz), and (c) swell-sea ($0.050 < f < 0.250$ Hz) significant wave heights, where f is frequency.

range errors owing to multiple reflections from the water surface near steep wave fronts (Vousdoukas et al. 2014), causing an increased time of flight and underestimation of the water elevation. Finally, small changes in position and orientation of the scanner can occur, especially during high wind conditions when the lidar is mounted on the top of a tall tower, but they are difficult to

measure using motion-sensing equipment. An un-accounted for cross-shore tilt of 0.01° would result in a vertical displacement of 0.02 m at 100-m range. Co-registration techniques on nonmoving portions of the scan could be used to remove these motions, but they were not applied here.

Missing returns can result from obstruction of the laser beam (by objects or people on the beach, a prior wave front, or rain and fog) or lack of foam on the water surface and the subsequent absorption or specular re-flection from flat or downward-sloped surfaces of the laser away from the scanner. Missing returns on the backside of a wave owing to obstruction by a prior wave front may result in overestimation of the sea surface when linearly interpolated, and could explain the lower wave heights (variance in water level) observed at g55 and g65. Lidar point separation for an angular resolu-tion of 0.02° on a horizontal plane at 0-m NAVD88 should increase from 0.02 m at g25 to 0.12 m at g65 (Fig. 7, cyan curve). The theoretical point separation on upward slopes (wave fronts) is smaller, whereas point separation on downward slopes (wave backsides) is larger. To estimate the actual lidar point separation, water surface slopes were used to identify and separate wave fronts and wave backsides, and the average (over all scans in a 20-min run) distance of the nearest point was calculated every 0.10 m (Fig. 7, blue and red dots). The theoretical flat-surface and observed point sepa-rations agree well between 0- and 40-m range, but the observed point separation increases more rapidly than the flat-surface spacing between 40- and 65-m range (the distance to the most offshore pressure gauge), reaching roughly 0.25 m for wave fronts (blue dots) and 0.40 m for wave backsides (red dots) (with a standard deviation of 0.85 m for both). At larger ranges, point separation increases farther and becomes scattered. For this example (Fig. 7), for distances less than (more than) 40 m, there was at least one measurement within each 0.10-m bin for 70%–100% (30%–60%) of the scans (including both fronts and backs of waves). The return rate within a given bin depends not only on instrument setup (grazing angle, angular resolution, distance offshore), type, and power, but also on envi-ronmental conditions (rain, fog, spray, wave height and steepness, foam) and was variable during the experi-ment. Coupled imagery in the red–green–blue or shortwave infrared band, which could see both the lidar beam and presence of foam, could help determine the causes of these dropouts. The lidar–pressure agree-ment did not degrade with distance offshore for the conditions considered here, and thus the linear inter-polation of the lidar data to the sensor locations does not appear to be a major source of error.
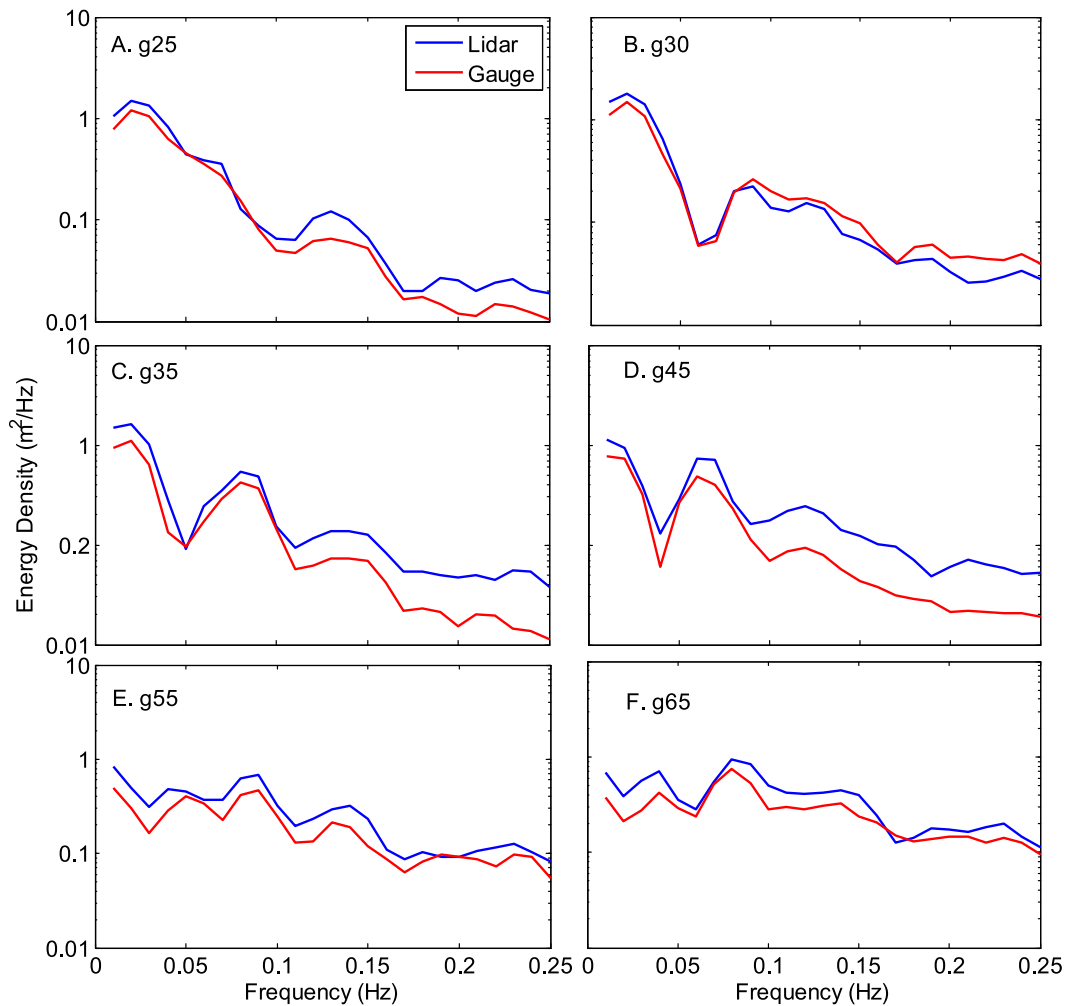
FIG. 5. Energy density vs frequency for the lidar (blue curves) and pressure gauges (red curves) during the 1700 EDT 5 Nov run for (a) g25, (b) g30, (c) g35, (d) g45, (e) g55, and (f) g65. There are approximately 40 degrees of freedom in the spectral estimates.

Potential sources of error in the pressure measurements include pressure sensor drifts and inaccurate transformation of the pressure data to sea surface elevations (owing to errors in the linear theory transformation or to inaccurate estimates of the sand level, and thus of water and burial depths). Pressure sensor drifts were estimated to be less than 0.02 m, based on comparison of lidar- and pressure-estimated sand levels when the beach was saturated, but uncovered by waves. The vertical locations of the gauges relative to the NAVD88 datum were surveyed accurately (± 0.02 m). However, the seafloor location was not always known well. The pressure gauges measure the height of water above the gauge, but they do not indicate what fraction of that depth is saturated sand. For example, for 1.0-m total measured water height above a gauge, at 0.2 Hz the estimated sea surface energy increases by 40% as burial

(ocean water) depths increase (decrease) from 0.0 (1.0) to 0.5 (0.5 m). Effects of changing burial depth increase with frequency (Raubenheimer et al. 1998). Thus, errors in the estimated bathymetry may contribute to differences in energy at high frequencies, including differences in swell–sea band significant wave heights. Pressure sensors could have been deployed within the water column, but flows past the pressure port would have caused dynamic pressure signals that are difficult to remove (e.g., "flow noise") (Raubenheimer et al. 2001), as well as increasing the likelihood of damage during storms.

Errors in the pressure measurements at the most onshore sensor also could be owing to the water table being below the sand surface (an unsaturated beach). Consistent with prior studies at this site (Turner and Masselink 1998), comparisons of the measured pressure
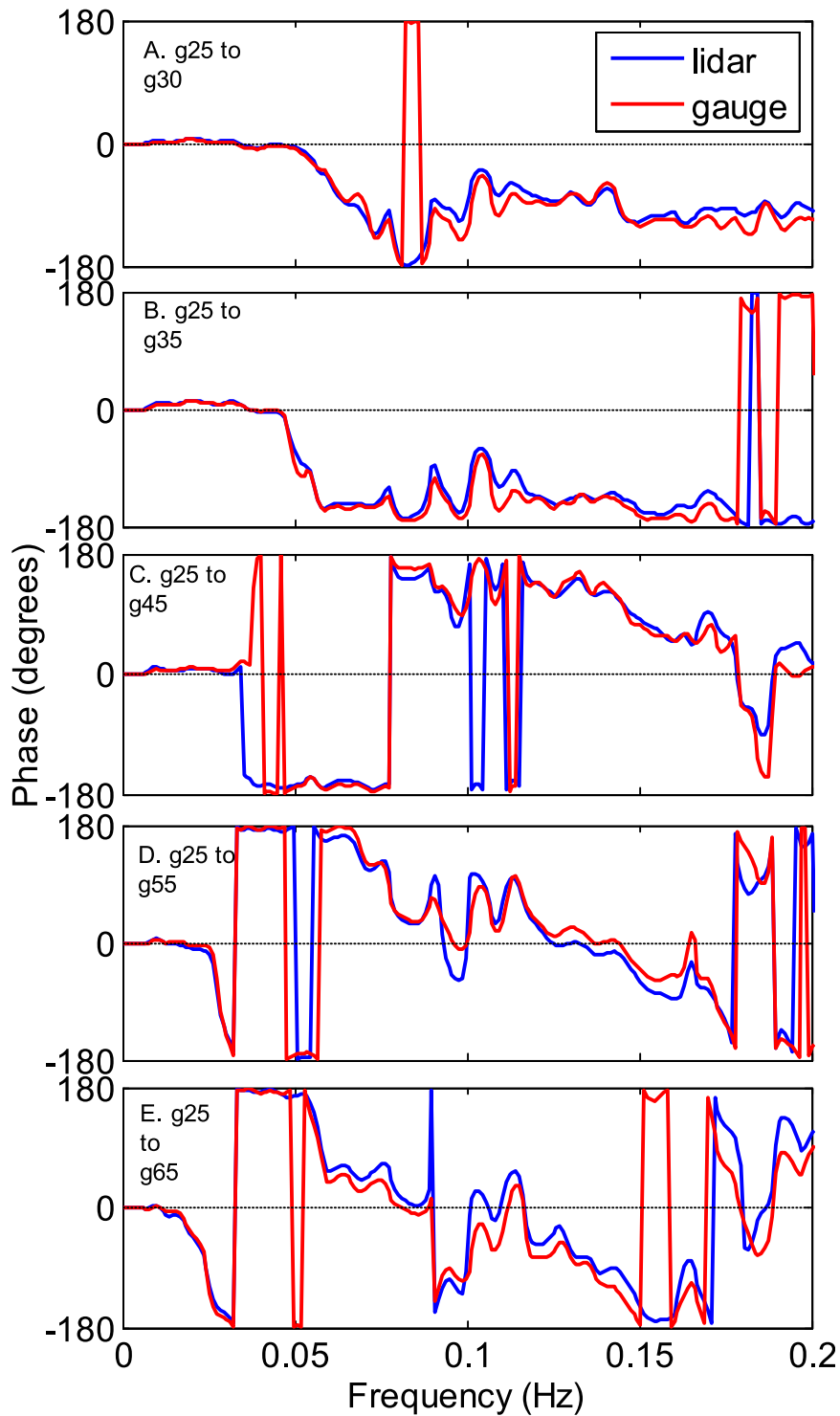
FIG. 6. Phase relative to the phase at g25 vs frequency during the 1700 EDT 5 Nov run for (a) g30, (b) g35, (c) g45, (d) g55, and (e) g65. Phases are between lidar observations (blue curves) and between pressure gauge observations (red curves).
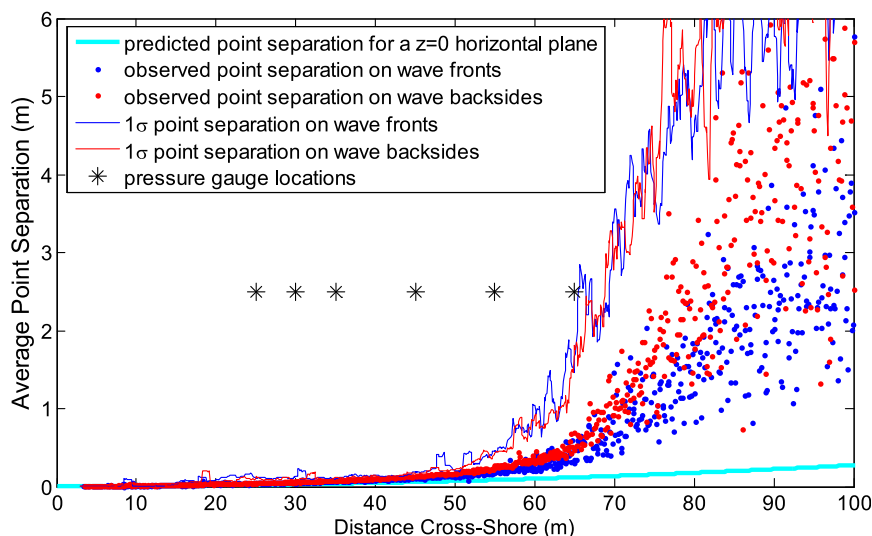
FIG. 7. Theoretical (cyan), run-averaged observed (dots), and standard deviation of observed (curves) lidar point separation estimated over 0.1-m bins vs distance cross-shore for wave fronts (blue dots) and wave backsides (red dots) during the 1700 EDT 5 Nov run. The black asterisks show cross-shore locations of the pressure gauges.

with the GPS beach surveys suggest the beach usually was saturated offshore of the mean swash location (and thus for the data used here). However, the beach may have been unsaturated in the lower swash under some conditions. If both the water table level and capillary fringe were below the beach surface, then there would be discrepancies between the lidar (which measures the water elevation above the beach) and pressure (which would measure the water in the saturated sand below the water table level). This situation would have resulted in smaller estimates of setup, water levels, and wave heights by g25 relative to the lidar, which is not consistent with the results (Fig. 4). However, if a capillary fringe extended from the water table to the beach surface, then a small amount of water could saturate the sediment (Gillham 1984), causing the observed pressure to increase rapidly, and possibly contribute to the high estimates of wave heights, and the occasional low estimates of mean water levels or setup, by g25 relative to the lidar.

During the large wave events, some of the pressure-sensor-mounting pipes were bent by floating debris, possibly affecting the measurements. Differences between the lidar and pressure measurements, separated by about 1 m in the alongshore, also could be owing to alongshore variability of the waves. Debris on the beach caused local scour and ponding, which may have exacerbated the alongshore variability in shallow water. Discrepancies between the lidar and pressure measurements also could be owing to foamy, aerated bores. In particular, foam could increase the elevation of the

surface measured by the lidar, while not affecting the pressure measured by the gauge.

Despite the potential sources of error in both pressure and lidar measurements of waves, the strong agreement between the two instruments (Table 1) suggests lidar data are of sufficient quality and accuracy to study inner-surfzone waves.

b. Potential applications of spatially dense lidar observations

The inner-surf and swash zone is where most storm impact and damage occurs, making it not only a critical region to study, but also a difficult location to maintain in situ gauges. Furthermore, the location of the inner surf and swash zone changes with tidal level, storm surge, and wave conditions, and thus it requires numerous in situ sensors to provide measurements spanning the area. The comparisons with pressure-gauge observations suggest that spatially dense lidar measurements could be used to examine wave propagation, including changing wave shapes and wave reflection, in this region. Examples are given below to illustrate some potential applications of lidar data and to evaluate the lidar for these uses.

As waves shoal and dissipate, wave shapes evolve owing to nonlinear energy exchanges and phase coupling. Changing wave shape affects velocity asymmetries, which can affect sediment transport magnitudes and directions, as well as impact forces on underwater structures. Positive wave skewness indicates sharper wave crests and flatter troughs, whereas positive asymmetry indicates
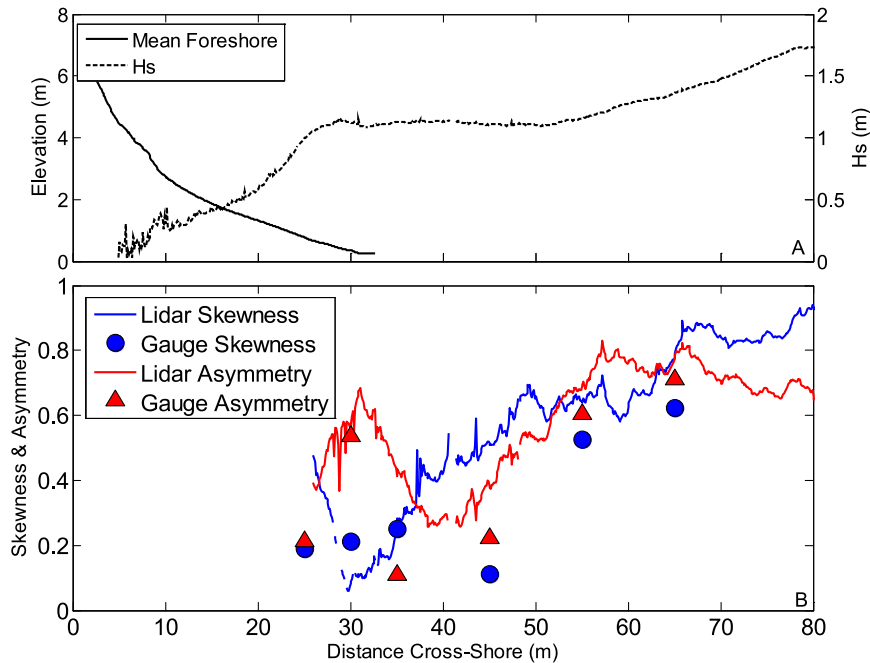
FIG. 8. Lidar-measured (a) beach profile (solid curve, left-hand *y* axis) and significant wave height (dashed curve, right-hand *y* axis) and (b) wave skewness (blue curve) and asymmetry (red curve) vs cross-shore distance for the 1700 EDT 5 Nov run. Pressure-based estimates of wave skewness (blue circles) and asymmetry (red triangles) also are shown in (b). Lidar estimates of skewness and asymmetry were calculated only for distances seaward of the swash zone.

steep front faces and more gently sloped rear faces (Masuda and Kuo 1981; Elgar and Guza 1985a; Doering and Bowen 1995). The cross-shore trends in pressure- and lidar-based skewness and asymmetry qualitatively are consistent with each other, and with earlier results. For example, the pressure- and lidar-based total skewness ($0.004 < f < 0.250$ Hz) decreases across the inner surf (Fig. 8b, blue curve and symbols; Elgar and Guza 1985b). The lidar- and pressure-based total asymmetry roughly is constant as wave heights decay between distance = 80 and 55 m, and then decreases onshore before a sharp increase near distance = 30 m, coincident with the slight increase in wave height (Fig. 8a; Raubenheimer et al. 1995), possibly related to nonlinear energy transfers as waves shoal on the steep foreshore prior to a shorebreak. Similar to the gently sloping beach results (Raubenheimer et al. 1995), the total shapes are affected by infragravity energy, and the swell–sea skewness and asymmetry are roughly uniform across the inner surf for distances greater than 30 m (not shown). The high spatial resolution of lidar-based estimates of asymmetry and skewness show localized variations not previously observed with more coarsely spaced pressure gauges, and may be related to small-scale bathymetric features in the cross-shore.

The lidar observations of the water surface also could be used to investigate wave shape as a function of breaking type (e.g., spilling or plunging) and its potential effect on sediment transport, wave run-up, and setup at the shoreline.

The energy density spectra (Fig. 5) at the gauge locations and cross-spectra between locations (Fig. 6) indicate the presence of standing waves at low frequencies (with associated nodes and antinodes in energy and 180° changes in phase between cross-shore-separated sensors). Progressive waves occur at higher frequencies, with energy that decays onshore and phases (relative to the shallowest sensor) that increase roughly linearly with increasing frequency. The lidar measurements enable high-spatial-resolution estimates of cross-shore wave transformation. In particular, the lidar spectra (Fig. 9) indicate that the nodal structure associated with standing waves may affect energy levels to frequencies of 0.1 Hz (Fig. 9, alternating red and blue with either increasing frequency at a fixed cross-shore location or with increasing cross-shore distance at a fixed frequency). Examination of the spatial- and frequency-dependent changes in nodal locations may be useful for understanding the structure of standing edge waves on a sloping beach (Suhayda 1974; Oltman-Shay and Guza
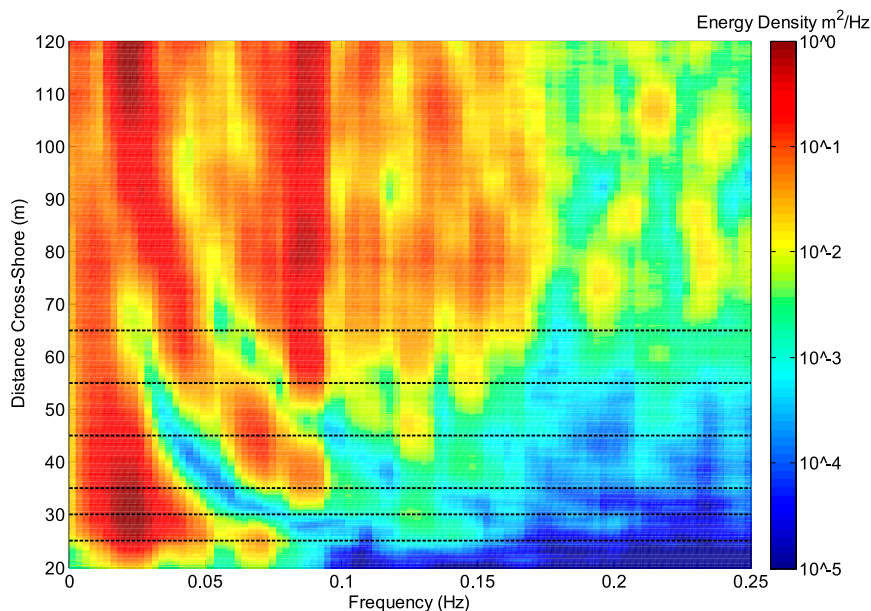
FIG. 9. Contours (scale on the right) of lidar-estimated energy density as a function of cross-shore distance and frequency during the 1700 EDT 5 Nov run. The horizontal dashed lines indicate the locations of the buried pressure gauges.

1987; Bryan and Bowen 1996; Johnson 2007) and for estimating wave reflection from beaches.

The cross-shore structure of mode 0–3 edge waves and of leaky waves was estimated over the measured bathymetry (Suhayda 1974; Oltman-Shay and Guza 1987; Bryan and Bowen 1996; Johnson 2007), with shoreline locations and shoreline energy densities crudely fit to the observations. Although the edge wave mode mix cannot be determined without alongshore observations, the lidar-based energy density levels are consistent with the theoretical cross-shore structure of a mode 3 edge wave (or a leaky wave, which has a similar structure to that for a mode 3 wave at these frequencies for these locations near the shoreline; Fig. 10). In particular, the locations of nodes (minima in energy density) and antinodes (maxima) agree qualitatively with theory. At higher frequencies (Figs. 10a,b), in addition to the standing wave structure, energy levels increase (approximated as a linear slope) with distance offshore, consistent with superposition of standing and progressive waves. However, the amplitude of the fluctuations in energy density is larger than would be expected for a mode 3 edge wave (or for a combination of mode 0–3 edge waves, not shown), possibly owing to the importance of nonlinearities in these shallow depths or to trapping of certain modes over the nearly flat cross-shore profile in the inner surf (distance > 40 m; Fig. 1). These relatively large spatial energy fluctuations may be associated with large convergences and divergences of

currents, and thus of sediment transport, leading to evolution of inner-surf morphology (Bowen and Inman 1971; Guza and Inman 1975; Holman and Bowen 1982; Guza and Thornton 1985; Holman and Sallenger 1985; Yu and Mei 2000). When coupled with other observations (from either lidar or pressure) in the alongshore, these results suggest high-resolution lidar data can be used to investigate edge wave structure and its effect on morphological evolution of the shoreline.

The frequency-dependent shoreline reflection coefficient (ratio of outgoing to incoming energy) can be estimated using measurements of sea surface fluctuations at multiple locations (Mansard and Funke 1980; Baldock and Simmonds 1999; Chang 2002; Chang and Hsu 2003; Wang et al. 2008). Here, reflection coefficients as a function of frequency were estimated from spectra calculated for 1024-s sea surface fluctuation time series measured at two locations separated in the cross-shore [Goda and Suzuki 1977, Eq. (5)]. Although this method does not account for the sloping bottom or wave obliquity, the results are comparable with prior field-based estimates. Furthermore, the seafloor slope was small for $40 < \text{cross-shore distance} < 76 \, \text{m}$ (Fig. 1). The cross-shore separation distance Δl for the two time series must fall in the range $0.05 \leq \Delta l/\lambda \leq 0.45$ (Goda and Suzuki 1977), where λ is the wavelength calculated from the frequency and the mean water depth. To cover a broad range of frequencies (wavelengths), sea surface time series for cross-shore distances 50, 62, 66, 68, and 76 m
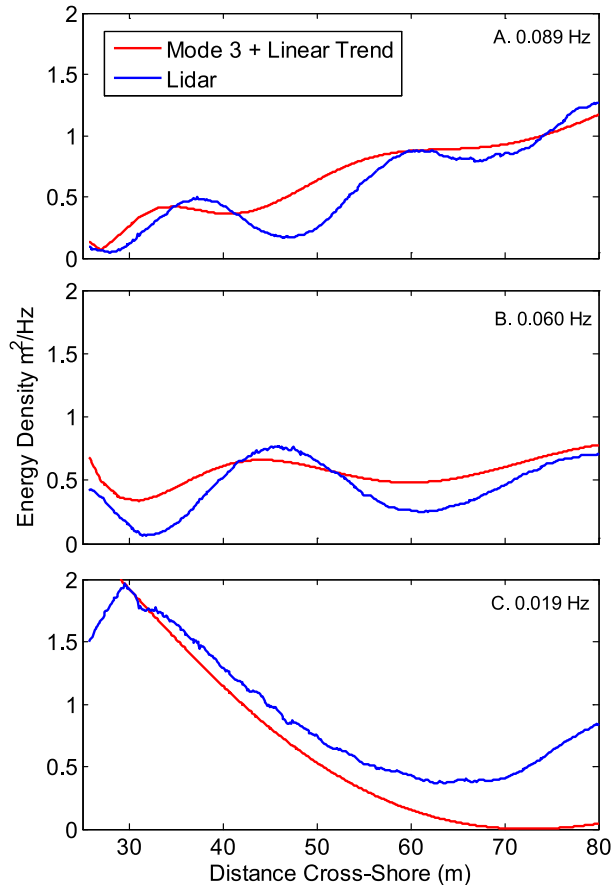
FIG. 10. Lidar-based (blue curves) and theoretical mode 3 edge wave (red curves) energy density vs cross-shore distance for frequencies (a) 0.089, (b) 0.060, and (c) 0.019 Hz.
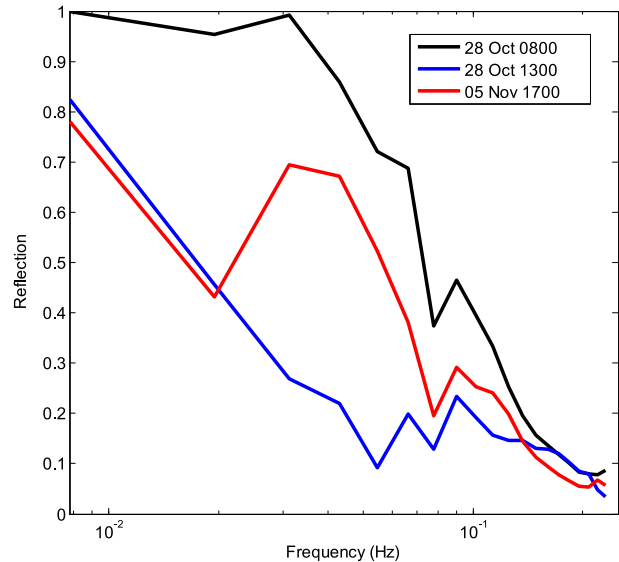

FIG. 11. Reflection coefficients estimated from lidar measurements vs frequency for the 0800 EDT 28 Oct run (black curve, foreshore slope = 0.14, offshore H_s = 2 m), 1300 EDT 28 Oct run (blue curve, foreshore slope = 0.04, offshore H_s = 2 m), and 1700 EDT 5 Nov run (red curve, foreshore slope = 0.17, offshore H_s = 3 m). Foreshore slopes are the average beach slope between the maximum run-up and minimum run-down measured by the lidar during each run.

were used to obtain spatial lags of 2, 4, 6, 8, 10, 12, 14, 16, 18, and 26 m. The reflection coefficients were estimated at each frequency by averaging results for four 256-s blocks of data using the pair of measurements with a spatial separation in the middle of the target range. The resulting coefficients (Fig. 11) were averaged over three neighboring frequencies to reduce statistical noise. Consistent with monochromatic wave theory (Miche 1951; Battjes 1975; Guza and Bowen 1976; Kobayashi and Watson 1987) and with prior field estimates (Suhayda 1974; Raubenheimer and Guza 1996; Huntley et al. 1999), the reflection coefficients for a particular run typically decrease with increasing frequency (Fig. 11), and at a given frequency increase with increasing beach slope (Fig. 11, compare blue curve with black curve) and with decreasing wave height (Fig. 11, compare red curve with black curve). Consistent with the cross-shore structure of energy density (Fig. 10), and with previous studies, the results suggest that reflection of infragravity waves can be high, especially for smaller waves and steeper slopes (Fig. 11, black curve), and that dissipating

shoreward-propagating waves become relatively more important at higher frequencies. The ability to measure simultaneous bed-level changes and wave reflection with the lidar data may help determine why morphology models have decreased skill predicting shoreline morphodynamics on steep, reflective beaches (Vousdoukas et al. 2011).

5. Conclusions

Water levels (r^2 = 0.98, rmse = 0.05 m), setup (r^2 = 0.92, rmse = 0.03 m), infragravity wave heights (r^2 = 0.91, rmse = 0.03 m), swell–sea wave heights (r^2 = 0.87, rmse = 0.07 m), and energy density spectra in the inner surf and swash on a sandy ocean beach estimated with 1550-nm low-grazing angle lidar measurements agree well with those estimated with buried pressure sensors. The lowest observed correlation (r^2 = 0.77) and the highest mean bias (0.10 m) occurred for swell–sea band waves at the shallowest wave gauge. These differences could be related to unsaturated beach conditions; foamy aerated bores that add height, but not weight, to the water column; or to multiple reflections from the mirror-like wet foreshore. Wave and water-level observations did not degrade with range, suggesting that for narrow-beam scanners (0.3 mrad), spatially variable spot size and linear interpolation over gaps in returns are not a large source of

error for these conditions. The maximum range of the lidar observations and percentage of pulses returned were dependent on environmental conditions (foam, wave heights, rain, fog, spray), with the maximum range for this scanner over this time period reaching 150 m. The lidar and pressure observations indicate that standing infragravity waves dominate the energy at low frequencies and progressive swell–sea waves dominate at higher frequencies, consistent with prior studies. Reflection coefficients, estimated from lidar measurements at pairs of locations with different spatial lags to cover a wide range of frequencies (or wavelengths), are high at low frequencies, increase with beach slope, and decrease with increasing offshore wave height. Lidar data suggest that wave asymmetry increases rapidly just offshore of the swash. Drawbacks to the lidar include degraded performance during heavy rain and the potential for rectification errors at far range from uncorrected sensor movement. The comparisons with pressure measurements presented here, prior studies, and theory demonstrate that lidar measures inner-surf waves and setup accurately, and can be a useful tool for investigating inner-surf and swash zone hydrodynamics.

REFERENCES

Aagaard, T., and B. Greenwood, 1994: Suspended sediment transport and the role of infragravity waves in a barred surf zone. *Mar. Geol.*, **118**, 23–48, doi:10.1016/0025-3227(94)90111-2.

Almeida, L. P., G. Masselink, P. E. Russell, M. Davidson, T. Poate, R. Mccall, C. Blenkinsopp, and I. L. Turner, 2013: Observations of the swash zone on a gravel beach during a storm using a laser-scanner (Lidar). *J. Coastal Res.*, **65**, 636–641, doi:10.2112/SI65-108.1.

Apotsos, A., B. Raubenheimer, S. Elgar, and R. T. Guza, 2008: Wave-driven setup and alongshore flows observed onshore of a submarine canyon. *J. Geophys. Res.*, **113**, C07025, doi:10.1029/2007JC004514.

Baldock, T. E., and D. J. Simmonds, 1999: Separation of incident and reflected waves over sloping bathymetry. *Coastal Eng.*, **38**, 167–176, doi:10.1016/S0378-3839(99)00046-0.

Battjes, J. A., 1975: Surf similarity. *Proceedings of the 14th Conference on Coastal Engineering*, Vol. 1, ASCE, 466–480.

——, and M. J. F. Stive, 1985: Calibration and verification of a dissipation model for random breaking waves. *J. Geophys. Res.*, **90**, 9159–9167, doi:10.1029/JC090iC05p09159.

Beach, R. A., and R. W. Sternberg, 1988: Suspended sediment transport in the surf zone: Response to cross-shore infragravity motion. *Mar. Geol.*, **80**, 61–79, doi:10.1016/0025-3227(88)90072-2.

Blenkinsopp, C. E., M. A. Mole, I. L. Turner, and W. L. Peirson, 2010: Measurements of the time-varying free-surface profile across the swash zone obtained using an industrial LIDAR. *Coastal Eng.*, **57**, 1059–1065, doi:10.1016/j.coastaleng.2010.07.001.

——, I. L. Turner, M. J. Allis, W. L. Peirson, and L. E. Garden, 2012: Application of LiDAR technology for measurement of time-varying free-surface profiles in a laboratory wave flume. *Coastal Eng.*, **68**, 1–5, doi:10.1016/j.coastaleng.2012.04.006.

Bowen, A. J., and D. L. Inman, 1971: Edge waves and crescentic bars. *J. Geophys. Res.*, **76**, 8662–8671, doi:10.1029/JC076i036p08662.

Brodie, K. L., R. K. Slocum, and J. E. McNinch, 2012: New insights into the physical drivers of wave runup from a continuously operating terrestrial laser scanner. *2012 Oceans*, IEEE, 8 pp., doi:10.1109/OCEANS.2012.6404955.

Bryan, K. R., and A. J. Bowen, 1996: Edge wave trapping and amplification on barred beaches. *J. Geophys. Res.*, **101**, 6543–6552, doi:10.1029/95JC03627.

Chang, H. K., 2002: A three-point method for separating incident and reflected waves over a sloping bed. *China Ocean Eng.*, **16**, 499–512.

——, and T. W. Hsu, 2003: A two-point method for estimating wave reflection over a sloping beach. *Ocean Eng.*, **30**, 1833–1847, doi:10.1016/S0029-8018(03)00017-9.

Doering, J. C., and A. J. Bowen, 1995: Parameterization of orbital velocity asymmetries of shoaling and breaking waves using bispectral analysis. *Coastal Eng.*, **26**, 15–33, doi:10.1016/0378-3839(95)00007-X.

Elgar, S., and R. T. Guza, 1985a: Observations of bispectra of shoaling surface gravity waves. *J. Fluid Mech.*, **161**, 425–448, doi:10.1017/S0022112085003007.

——, and ——, 1985b: Shoaling gravity waves: Comparisons between field observations, linear theory, and a nonlinear model. *J. Fluid Mech.*, **158**, 47–70, doi:10.1017/S0022112085002543.

Gillham, R. W., 1984: The capillary fringe and its effect on water-table response. *J. Hydrol.*, **67**, 307–324, doi:10.1016/0022-1694(84)90248-8.

Goda, Y., and Y. Suzuki, 1977: Estimation of incident and reflected waves in random wave experiments. *Proceedings of the 15th Coastal Engineering Conference*, Vol. 1, ASCE, 828–845.

Guza, R. T., and D. L. Inman, 1975: Edge waves and beach cusps. *J. Geophys. Res.*, **80**, 2997–3012, doi:10.1029/JC080i021p02997.

——, and A. J. Bowen, 1976: Resonant interactions for waves breaking on a beach. *Proceedings of the 15th Conference on Coastal Engineering*, Vol. 1, ASCE, 560–579.

——, and E. B. Thornton, 1982: Swash oscillations on a natural beach. *J. Geophys. Res.*, **87**, 483–491, doi:10.1029/JC087iC01p00483.

——, and ——, 1985: Observations of surf beat. *J. Geophys. Res.*, **90**, 3161–3172, doi:10.1029/JC090iC02p03161.

Haas, K. A., I. A. Svendsen, M. C. Haller, and Q. Zhao, 2003: Quasi-three dimensional modeling of rip current systems. *J. Geophys. Res.*, **108**, 3217, doi:10.1029/2002JC001355.

Haller, M. C., R. A. Dalrymple, and I. A. Svendsen, 2002: Experimental study of nearshore dynamics on a barred beach with rip channels. *J. Geophys. Res.*, **107**, 3061, doi:10.1029/2001JC000955.

Hansen, J., T. T. Janssen, B. Raubenheimer, F. Shi, P. Barnard, and I. Jones, 2014: Observations of surfzone alongshore pressure gradients onshore of an ebb-tidal delta. *Coastal Eng.*, **91**, 251–260, doi:10.1016/j.coastaleng.2014.05.010.

Holman, R. A., and A. J. Bowen, 1982: Bars, bumps and holes: Models for the generation of complex beach topography. *J. Geophys. Res.*, **87**, 457–468, doi:10.1029/JC087iC01p00457.

——, and A. H. Sallenger, 1985: Setup and swash on a natural beach. *J. Geophys. Res.*, **90**, 945–953, doi:10.1029/JC090iC01p00945.

Holman, R., A. Sallenger, T. Lippmann, and J. Haines, 1993: The application of video image processing to the study of nearshore processes. *Oceanography*, **6**, 78–85, doi:10.5670/oceanog.1993.02.

Houser, C., and B. Greenwood, 2007: Onshore migration of a swash bar during a storm. *J. Coastal Res.*, **23**, 1–14, doi:10.2112/03-0135.1.

——, ——, and T. Aagaard, 2006: Divergent response of an intertidal swash bar. *Earth Surf. Processes Landforms*, **31**, 1775–1791, doi:10.1002/esp.1365.

Howd, P. A., and R. A. Holman, 1987: A simple model of beach foreshore response to long-period waves. *Mar. Geol.*, **78**, 11–22, doi:10.1016/0025-3227(87)90065-X.

Huntley, D. A., D. Simmonds, and R. Tatavarti, 1999: Use of collocated sensors to measure coastal wave reflection. *J. Waterw. Port Coastal Ocean Eng.*, **125**, 46–52, doi:10.1061/(ASCE)0733-950X(1999)125:1(46).

Jafari, A., N. Cartwright, and P. Nielsen, 2012: Manometer tubes for monitoring coastal water levels: New frequency response factors. *Coastal Eng.*, **66**, 35–39, doi:10.1016/j.coastaleng.2012.03.010.

Johnson, R. S., 2007: Edge waves: theories past and present. *Philos. Trans. Roy. Soc. London*, **365A**, doi:10.1098/rsta.2007.2013.

King, B. A., M. W. L. Blackley, A. P. Carr, and P. J. Hardcastle, 1990: Observations of wave-induced setup on a natural beach. *J. Geophys. Res.*, **95**, 22 289–22 297, doi:10.1029/JC095iC12p22289.

Kobayashi, N., and K. D. Watson, 1987: Wave reflection and runup on smooth slopes. *Coastal Hydrodynamics: Proceedings of a Conference Sponsored by the Waterway, Port, Coastal and Ocean Division of the American Society of Civil Engineers*, R. A. Dalrymple, Ed., ASCE, 548–563.

——, and H. Jung, 2012: Beach erosion and recovery. *J. Waterw. Port Coastal Ocean Eng.*, **138**, 473–483, doi:10.1061/(ASCE)WW.1943-5460.0000147.

Lentz, S., and B. Raubenheimer, 1999: Field observations of wave setup. *J. Geophys. Res.*, **104**, 25 867–25 875, doi:10.1029/1999JC900239.

Mansard, E. P. D., and E. R. Funke, 1980: The measurement of incident and reflected spectra using a least squares method. *17th International Conference on Coastal Engineering*, B. L. Edge, Ed., ASCE, 154–172.

Masselink, G., and S. van Heteren, 2014: Response of wave-dominated and mixed-energy barriers to storms. *Mar. Geol.*, **352**, 321–347, doi:10.1016/j.margeo.2013.11.004.

Masuda, A., and Y.-Y. Kuo, 1981: A note on the imaginary part of bispectra. *Deep-Sea Res.*, **28A**, 213–222, doi:10.1016/0198-0149(81)90063-7.

Miche, R., 1951: Le pouvoir réfléchissant des ouvrages maritimes exposés à l'action de la houle. *Ann. Ponts Chaussees*, **121**, 285–319.

Morel, A., 1974: Optical properties of pure water and pure sea water. *Optical Aspects of Oceanography*, N. G. Jerlov and E.S. Nielson, Eds., Academic Press Inc., 1–24.

Nielsen, P., 1988: Wave setup: A field study. *J. Geophys. Res.*, **93**, 15 643–15 652, doi:10.1029/JC093iC12p15643.

Oltman-Shay, J., and R. T. Guza, 1987: Infragravity edge wave observations on two California beaches. *J. Phys. Oceanogr.*, **17**, 644–663, doi:10.1175/1520-0485(1987)017<0644:IEWOOT>2.0.CO;2.

Puleo, J. A., and Coauthors, 2014: A comprehensive field study of swash-zone processes. I: Experimental design with examples of hydrodynamic and sediment transport measurements. *J. Waterw. Port Coastal Ocean Eng.*, **140**, 14–28, doi:10.1061/(ASCE)WW.1943-5460.0000210.

Putrevu, U., J. Oltman-Shay, and I. A. Svendsen, 1995: Effect of alongshore nonuniformities on longshore current predictions. *J. Geophys. Res.*, **100**, 16 119–16 130, doi:10.1029/95JC01459.

Raubenheimer, B., and R. T. Guza, 1996: Observations and predictions of run-up. *J. Geophys. Res.*, **101**, 25 575–25 587, doi:10.1029/96JC02432.

——, ——, S. Elgar, and N. Kobayashi, 1995: Swash on a gently sloping beach. *J. Geophys. Res.*, **100**, 8751–8760, doi:10.1029/95JC00232.

——, S. Elgar, and R. T. Guza, 1998: Estimating wave heights from pressure measured in a sand bed. *J. Waterw. Port Coast. Ocean Eng.*, **124**, 151–154, doi:10.1061/(ASCE)0733-950X(1998)124:3(151).

——, R. T. Guza, and S. Elgar, 2001: Field observations of wave-driven setdown and setup. *J. Geophys. Res.*, **106**, 4629–4638, doi:10.1029/2000JC000572.

Sallenger, A. H., Jr., 2000: Storm impact scale for barrier islands. *J. Coastal Res.*, **16**, 890–895.

Stockdon, H. F., A. H. Sallenger, R. A. Holman, and P. A. Howd, 2007: A simple model for the spatially-variable coastal response to hurricanes. *Mar. Geol.*, **238**, 1–20, doi:10.1016/j.margeo.2006.11.004.

Streicher, M., B. Hofland, and R. C. Linderbergh, 2013: Laser ranging for monitoring water waves in the new Deltares Delta Flume. *ISPRS Workshop Laser Scanning 2013*, M. Scaioni et al., Eds., Vol. II-5/W2, ISPRS, 265–270.

Suhayda, J. N., 1974: Standing waves on beaches. *J. Geophys. Res.*, **79**, 3065–3071, doi:10.1029/JC079i021p03065.

Turner, I. L., and G. Masselink, 1998: Swash infiltration-exfiltration and sediment transport. *J. Geophys. Res.*, **103**, 30 813–30 824, doi:10.1029/98JC02606.

van Rooijen, A. Reniers, J. van Thiel de Vries, C. Blenkinsopp, and R. McCall, 2012: Modeling swash zone sediment transport at Truc Vert Beach. *33rd Conference on Coastal Engineering 2012*, P. Lynett and J. McKee Smith, Eds., Vol. 4, ICCE, 3265–3276.

Vousdoukas, M. I., L. P. Almeida, and Ó. Ferreira, 2011: Modelling storm-induced beach morphological change in a meso-tidal, reflective beach using XBeach. *J. Coastal Res.*, **64**, 1960–1920.

——, T. Kirupakaramoorthy, H. Oumeraci, M. de la Torre, F. Wübbold, B. Wagner, and S. Schimmels, 2014: The role of combined laser scanning and video techniques in monitoring wave-by-wave swash zone processes. *Coastal Eng.*, **83**, 150–165, doi:10.1016/j.coastaleng.2013.10.013.

Wang, S.-K., T.-W. Hsu, W.-K. Weng, and S.-H. Ou, 2008: A three-point method for estimating wave reflection of obliquely incident waves over a sloping bottom. *Coastal Eng.*, **55**, 125–138, doi:10.1016/j.coastaleng.2007.09.002.

Yu, J., and C. C. Mei, 2000: Formation of sand bars under surface waves. *J. Fluid Mech.*, **416**, 315–348, doi:10.1017/S0022112000001063.